Nanoscale

PAPER

View Article Online
View Journal

Cite this: DOI: 10.1039/d5nr05265c

Carbon-encapsulated PtPd alloy electrocatalysts on single-walled carbon nanotubes for durable polymer electrolyte fuel cells

Miftakhul Huda, *[a] Tomoya Kawahara,[a] Chu-Yang Yu,[a] Yasuyuki Sawada,[b] Nagahiro Saito, [a,b] Masaya Kawasumi*[a,b] and Yutaka Matsuo *[a,b]

Highly crystalline single-walled carbon nanotubes were employed as robust supports for carbon-encapsulated PtPd alloy electrocatalysts synthesized *via* a rapid, industrially scalable solution plasma method, enhancing long-term durability under frequent start-up/shut-down conditions. Electrochemical evaluation of PtPd@C/SWCNT as a cathode catalyst in a polymer electrolyte fuel cell (PEFC) membrane electrode assembly (MEA) demonstrated superior durability compared to commercial Pt/C and monometallic Pt@C/SWCNT under an accelerated durability test. PtPd@C/SWCNT maintained high performance for 5000 potential cycles and retained over 50% of its electrochemically active surface area (ECSA) after 10 000 cycles under the accelerated durability test of high-potential triangular pulses (1.0–1.5 V) simulating harsh conditions encountered during actual start-up/shut-down operations. Carbon encapsulation effectively inhibited nanoparticle agglomeration and suppressed the oxidation of the SWCNT support in close proximity to the nanoparticles during the durability test of 30 000 cycles. Raman spectroscopy confirmed the excellent corrosion resistance and maintained the crystallinity of the SWCNT support. The negligible thickness change observed in the PtPd@C/SWCNT cathode layer further highlights the benefit of the SWCNT support and carbon encapsulation in maintaining structural integrity under severe operating conditions. XPS analysis indicated a more stable, reduced state of Pt in PtPd@C/SWCNT compared to that of Pt/C. These results highlight the synergistic effects of the SWCNT support and carbon encapsulation in improving both catalyst stability and support durability for prolonged PEFC operation, particularly under demanding heavy-duty vehicle (HDV) conditions.

Received 15th December 2025,
Accepted 12th May 2026

DOI: 10.1039/d5nr05265c

rsc.li/nanoscale

1. Introduction

Polymer electrolyte fuel cells (PEFCs) are emerging as a promising energy conversion technology for achieving carbon neutrality, thanks to their exceptional energy conversion efficiency, high power density, and environmental sustainability.[1–3] As a green technology for long-term use, PEFCs utilize hydrogen and oxygen (or air) as fuels, producing only water and heat, without emitting harmful gases such as CO_2 and CO. Despite the commercialization of PEFC technologies, ongoing research remains crucial to develop high-performance and highly durable PEFC devices, particularly for demanding applications like heavy-duty vehicles.[4,5] Platinum (Pt) is widely recognized as the most effective catalyst for the sluggish oxygen reduction reaction (ORR) that occurs at the cathode electrode in PEFCs.[6,7] However, the durability of Pt electrocatalysts and their supporting materials remains a major challenge limiting the widespread application of PEFCs.[7–9] Pt electrocatalysts are susceptible to dissolution and aggregation during long-term operation under the harsh conditions within a fuel cell.[10–12] Simultaneously, conventional carbon support materials can undergo corrosion and structural degradation during actual operation, which often involves harsh conditions and frequent dynamic changes such as fuel starvation and repeated start-up/shut-down cycles over extended use.[13,14] In particular, the anticipated deployment of PEFCs in heavy-duty vehicles in the near future necessitates superior durability and performance for both the metallic catalysts and their carbon supports to withstand demanding operational conditions.[5,15]

Carbon nanotubes (CNTs) are well known for their exceptional properties, including high electrical conductivity, high crystallinity, and high porosity.[16,17] The high conductivity and

[a]*Department of Chemical Systems Engineering, Graduate School of Engineering, Nagoya University, Nagoya 464-8603, Japan.*
E-mail: miftakhul.huda.j7@f.mail.nagoya-u.ac.jp, kawasumi.masaya.e1@f.mail.nagoya-u.ac.jp, matsuo.yutaka.h7@f.mail.nagoya-u.ac.jp
[b]*Institute of Materials Innovation, Institutes of Innovation for Future Society, Nagoya University, Nagoya 464-8601, Japan*

porosity of CNTs are anticipated to enhance the performance of PEFCs, while their high crystallinity, coupled with an inert surface, is expected to provide significant oxidation resistance, thereby improving durability under harsh operating conditions.[18–21] Recently, an enhanced direct injection pyrolytic synthesis (e-DIPS) method has enabled the synthesis of single-walled carbon nanotubes (SWCNTs) with a uniform thin diameter, high crystallinity, and low impurity levels.[22] The uniform and thin diameter (1–2 nm) of e-DIPS SWCNTs contributes to their high porosity, while their high crystallinity, evidenced by a high G/D ratio (>160) in Raman spectroscopy, suggests excellent durability.[22,23] Moreover, the high proportion of metallic over semiconducting CNTs within e-DIPS SWCNTs results in low electronic resistance. Consequently, the use of e-DIPS SWCNTs as a support material in PEFC applications holds promise for improving both performance and durability.

Despite the generally inert surface of SWCNTs, our prior work demonstrated the successful synthesis of Pt electrocatalysts directly onto e-DIPS SWCNTs without the need for templates, linkers, or surface modifications, which can often hinder subsequent applications.[24] The use of e-DIPS SWCNTs, provided by Meijo Nano Carbon Co., Ltd, as a support material for Pt electrocatalysts has been shown to enhance PEFC durability.[25,26] In this study, e-DIPS SWCNTs were employed as a support to synthesize PtPd alloy electrocatalysts encapsulated by a carbon shell (PtPd@C/SWCNT) using the solution plasma (SP) method. For comparison, a Pt@C/SWCNT electrocatalyst was synthesized and characterized using the same procedure as that employed for PtPd@C/SWCNT. SP is a rapid and efficient route for nanostructure synthesis, conducted at room temperature and ambient pressure, making it cost-effective and highly amenable for industrial scale-up.[27,28] Furthermore, the SP method offers an environmentally friendly process with minimal chemical usage, providing additional economic and sustainability benefits.[29] A series of carbon-encapsulated Pt-based alloy electrocatalysts were synthesized using SP. Our previous findings indicated that carbon-encapsulated PtPd alloy electrocatalysts supported on carbon black demonstrated superior durability and reactivity for the oxygen reduction reaction (ORR) compared to PtAu and PtAg alloy electrocatalysts.[30] In another study, the PtPd/C catalyst exhibited higher mass activity (MA) than commercial Pt/C and demonstrated excellent stability, retaining 96.5% of its MA after 10 000 cycles in a standard durability test involving linear potential pulses between 0.5 and 1.0 V.[31]

In this study, the synthesized PtPd@C/SWCNT and reference catalysts were used as cathode catalysts to fabricate membrane electrode assemblies (MEAs). Electrocatalyst stability is typically evaluated using two types of durability tests. One employs a rectangular potential pulse cycling between 0.6 and 0.95 V to simulate fuel cell operating conditions, accelerate Pt degradation, and assess long-term catalyst durability.[31–33] In this study, however, a high-potential triangular wave (1.0–1.5 V) durability test was chosen to specifically induce corrosion of the carbon support, including the supported metal nanoparticles.[34,35] This method aims to simulate harsh operating conditions encountered during frequent start-up/shut-down cycles. The PtPd@C/SWCNT catalyst maintained high performance for up to 5000 cycles under these demanding conditions and retained over 50% of its electrochemically active surface area (ECSA) up to 10 000 cycles. A range of structural and electronic characterization studies, including X-ray photoelectron spectroscopy (XPS), transmission electron microscopy (TEM), scanning electron microscopy (SEM), X-ray diffraction (XRD), and Raman spectroscopy measurements, were employed to elucidate the mechanism responsible for the high durability of PtPd@C/SWCNT as the cathode catalyst in a PEFC MEA under the high-potential durability test.

2. Experimental section

2.1. Materials

Pt–Pd alloy wire with a diameter of 0.5 mm containing Pt of 80 wt% and Pd of 20 wt% and Pt wire with the same diameter were purchased from Nilaco Co. *N*,*N*-Dimethylformamide (DMF, >99.5%), 5% Nafion™ dispersion solution DE521 CS type, ethanol (>99.5%), acetone (>99.5%), and methanol (>99.8%) were purchased from Fujifilm Wako Pure Chemical Co. and used as received. SWCNTs synthesized using e-DIPS with a carbon purity of >99% and a diameter of approximately 2 nm were provided by Meijo Nano Carbon Co., Ltd and used as received.[36] Perchloric acid ($HClO_4$, 70%) and 2-propanol (IPA, >99.7%) were purchased from Kanto Chemical Co. and used as received. Hydrophilic polytetrafluoroethylene (PTFE) membrane (0.2 μm pore size) was purchased from Merck. A commercial Pt/C catalyst (20 wt%, Pt nanocatalyst diameter <5 nm), *N*-methyl-2-pyrrolidone (NMP, 99.5%), and sodium dodecylbenzenesulfonate (SDBS) used as a dispersant of SWCNT-supported catalysts were purchased from Sigma-Aldrich and used as received.[37] Nafion membrane NRE-212 (thickness: 50 μm) was purchased from Moubic and used as received.

2.2. Methods

Low-magnification TEM images were obtained using a transmission electron microscope (JEOL, JEM-2100Plus) operated at an accelerating voltage of 200 kV. High resolution TEM images and EDS analysis were obtained using an aberration-corrected transmission electron microscope (JEOL, JEM-ARM200F Cold) equipped with an EDS analyzer (acceleration voltage of 200 kV). Cross-sectional SEM images of membrane electrode assemblies (MEAs) utilizing Pt@C/SWCNT and Pt/C as the cathode catalyst layer in the durability test were recorded using a FE-SEM JSM-7001F (JEOL) and a SUPRA 40VP (ZEISS), respectively. The samples for cross-sectional SEM measurements were prepared by cross-sectionally cutting MEAs using scissor manually and cryo argon ion-milling, respectively. X-ray photoelectron spectroscopy (XPS) measurements were carried out using an ESCALAB 250 (VG Scientific) with Al Kα radiation. The crystallinity of the electrocatalysts was characterized using

a Rigaku X-ray diffractometer (XRD, Rigaku SmartLab) with Cu Kα radiation (λ = 0.154 nm) operated at a voltage of 40 kV and current of 200 mA and the crystalline size of the electrocatalysts was calculated using the Scherrer formula.

X-ray absorption spectroscopy (XAS) was performed at the BL5S1 beamline of the Aichi Synchrotron Radiation Center (AichiSR), operated by the Aichi Science & Technology Foundation in Seto, Aichi, Japan (Proposal No. 202401026). This beamline consists of a superconducting magnet (5 T) as the light source, a flat-bent Rh-coated mirror for collimation, a Si (111) double-crystal monochromator, and a cylindrically bent Rh-coated mirror for focusing and filtering higher harmonics. The photon flux at the sample position was ≈3 × 10^{10} photons per second, with a spot size smaller than 0.5 mm × 0.5 mm. The photon energy calibration used the characteristic peak (8980.3 eV) in the Cu K-edge X-ray absorption near edge structure (XANES) spectrum of a Cu foil. Pt L_3-edge XANES spectra of samples were recorded in transmission mode using the Si (111) monochromator. The crystallinity of the SWCNTs was analyzed using Raman spectroscopy (Renishaw Plc., Leica DM 2500M Ren (RL/TL) microscope) with a laser-excitation wavelength of 532.5 nm. The mass compositions of the catalysts were determined by thermal gravimetric analysis (TGA, TGA&DTG-60AH, Shimadzu Co.) through annealing up to 1000 °C at a heating rate of 10 °C min^{-1} in air.

2.3. Preparation of PtPd@C/SWCNT

The SWCNT-supported PtPd alloy electrocatalysts encapsulated by a carbon shell (PtPd@C/SWCNT) were synthesized using the SP method as illustrated in Fig. 1.[30] SWCNTs (5 mg) were added into DMF (100 mL) and dispersed using an ultrasonicator for 15 minutes. Then, the solution was put into a glass reactor of SP. Bipolar pulse generated by a power supply (bipolar-DC pulsed power supply, Kurita Seisakusho Co., Ltd) was applied between a pair electrodes of PtPd alloy wires, which were placed with a distance of 0.5 mm. The SP synthesis was conducted in the DMF solution using a typical pulse with a voltage of 2 kV, frequency of 10 kHz, and a pulse width of 1.5 μm. The pulse to produce plasma in liquid was discharged for 40 minutes with breaks for two minutes every two minutes to maintain the temperature of the solution lower. The distance between the PtPd alloy wire electrodes was adjusted to 0.5 mm during the breaks. After SP synthesis, the PtPd@C/SWCNT electrocatalyst was collected on a PTFE membrane filter by filtration and washed with acetone, methanol, and pure water sequentially several times before drying at 80 °C overnight to remove excess solvents. The Pt@C/SWCNT electrocatalyst was prepared using the similar method, with Pt wires serving as the electrodes.

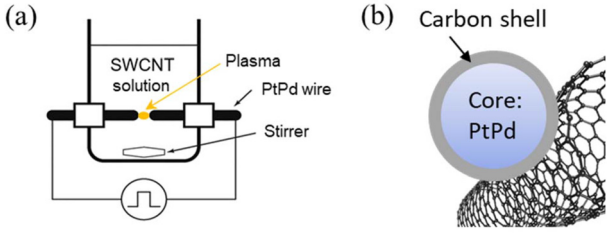

Fig. 1 Schematic images of (a) PtPd@C/SWCNT synthesis using the solution plasma method and (b) carbon-encapsulated PtPd alloy nanoparticles supported on SWCNTs.

2.4. ORR tests in the liquid half-cell

Electrochemical activity of the synthesized PtPd@C/SWCNT, Pt@C/SWCNT, and Pt/C electrocatalysts was evaluated using cyclic voltammetry (CV) and linear sweep voltammetry (LSV) techniques. The measurements were carried out using a standard three-electrode system with a bio-logic potentiostat/galvanostat (SP-150). A glassy carbon (GC) rotating disk electrode with a diameter of 5 mm (Pine Instrument), Pt coil, and reversible hydrogen electrode (RHE) were employed as the working, counter, and reference electrodes, respectively. A typical catalyst solution of commercial Pt/C was prepared by mixing Pt/C 20 wt% (5.3 mg), 5 wt% Nafion solution (16.2 μL), ultrapure water (85.7 μL), and IPA (3.3 mL), and followed by ultrasonication for 2 minutes. Then, the Pt/C catalyst solution (10 μL) was pipetted onto the GC surface, giving a Pt loading of 20.4 μg cm^{-2}. The catalyst on the GC surface was then allowed to dry at room temperature for 15 minutes before the electrochemical measurements.

Electrochemical measurements were performed at room temperature using a three-electrode setup in a 0.1 M $HClO_4$ electrolyte. Prior to the oxygen reduction reaction (ORR) studies, cyclic voltammetry (CV) activation was conducted in N_2-saturated 0.1 M $HClO_4$ at a scan rate of 50 mV s^{-1}. Then, the electrolyte was saturated with O_2 for 30 minutes, and CV measurements were recorded 50 times at 50 mV s^{-1} until a stable voltammogram was achieved. The electrochemically active surface area (ECSA) was determined by integrating the hydrogen adsorption charge in the stable-state CV under N_2 saturation, assuming a hydrogen monolayer adsorption charge of 210 μC cm^{-2} and a scan rate of 50 mV s^{-1}. Linear sweep voltammetry (LSV) measurements for ORR activity evaluation were conducted in O_2-saturated 0.1 M $HClO_4$ at a scan rate of 10 mV s^{-1} and a rotating disk electrode rotation speed of 1600 rpm.

2.5. MEA tests in a single fuel-cell

A membrane electrode assembly (MEA) with an electrode size of 1 cm^2 was fabricated by hot-pressing the cathode catalyst layer and an anode catalyst layer onto a Nafion membrane NRE-212 (50 μm thickness) under a pressure of 1.5 MPa at a temperature of 140 °C for 3 minutes. The cathode catalyst layer consisting of PtPd@C/SWCNTs was prepared using a membrane-filtration technique. To obtain a homogeneous catalyst solution, the PtPd@C/SWCNT catalyst (6 mg) was mixed with SDBS (6 mg), 5 wt% Nafion solution (78 μL), and ethanol (15 mL) and followed by ultrasonication for 15 minutes. The PtPd@C/SWCNT catalyst solution was filtered using a PTFE membrane filter and washed with acetone, methanol, and pure water sequentially multiple times to reduce the SDBS

content before drying at 80 °C overnight. The Pt loading of the membrane-filter coated with the PtPd@C/SWCNT catalyst layer was determined to be 108 μg cm^{-2} based on the TGA results. An anode catalyst layer of Pt/C was obtained by mixing Pt/C (10 mg), NMP (50 μL), 5 wt% Nafion solution (65 μL), and ethanol (400 μL) and followed by ultrasonication for 5 minutes. The Pt/C solution was drop-cast onto a Teflon sheet (1 cm^2) and dried at room temperature, giving a Pt loading of 365 μg cm^{-2}. For comparison, a referential MEA was prepared using the similar technique with Pt/C as the catalyst layers on both cathode and anode electrodes. An MEA with Pt@C/SWCNT as the cathode catalyst was fabricated following the similar procedure as the PtPd@C/SWCNT-based MEA.

The fabricated MEA was then set into a single fuel-cell (Chemix co. Ltd, FC-010-01H) and tested using a fuel cell test system (TOYO Corp.). Carbon paper (GDL-28-AA) as a gas diffusion layer, carbon plate as a bipolar plate, and a silicon gasket were used. Prior to all MEA measurements, a typical conditioning treatment was conducted to clean the surface catalyst and activate the catalyst by applying a constant voltage of 0.5 V under a cell temperature of 80 °C, anode (H_2, 139 NmL min^{-1}, relative humidity [RH] 81%), and cathode (air, 332 NmL min^{-1}, RH 81%) for 20 hours. *I–V* measurements were conducted under a cell temperature of 80 °C, anode (H_2, 1 NL min^{-1}, RH 100%), and cathode (air, 2 NL min^{-1}, RH 100%). These measurements were recorded several times until the stable highest current density was obtained. Prior to CV measurements, the cell was supplied with H_2 at a rate of 70 NmL min^{-1} on the anode and N_2 at a rate of 166 N mL min^{-1} on the cathode for 15 minutes. After the N_2 supply on the cathode was stopped, CV measurements were taken five times under a cell temperature of 80 °C and anode (H_2, 70 N mL min^{-1}, RH 100%) by scanning between 0.05 and 0.9 V with a scan rate of 50 mV s^{-1}, 5 times. The ECSA was calculated by assuming a value of 210 μC cm^{-2} for the adsorption of a hydrogen monolayer. A durability test (potential cycling) was conducted to simulate the deterioration of catalysts, especially the carbon support during start-up and shut-down operation of the fuel cell by applying a high-potential triangular pulse between 1.0 V and 1.5 V with 2 s per cycle under a cell temperature of 80 °C, anode (H_2, 70 N mL min^{-1}, RH 100%), and cathode (N_2, 166 N mL min^{-1}, RH 100%). *I–V* and CV measurements were conducted on several points during the durability test up to 30 000 cycles.

3. Results and discussion

A typical solution plasma (SP) method was used to synthesize the carbon-encapsulated PtPd alloy electrocatalyst supported on SWCNTs (PtPd@C/SWCNT). A PtPd alloy wire with a diameter of 0.5 mm was used to generate plasma within a DMF solution containing dispersed SWCNTs. The plasma was sustained for a total of 40 minutes to synthesize the PtPd@C/SWCNT catalyst with a Pt loading of 19.5 wt% (SI Fig. S1). The TEM images (Fig. 2(a)) show the synthesized nanoparticles with an average diameter of 2.3 ± 0.8 nm attached to the

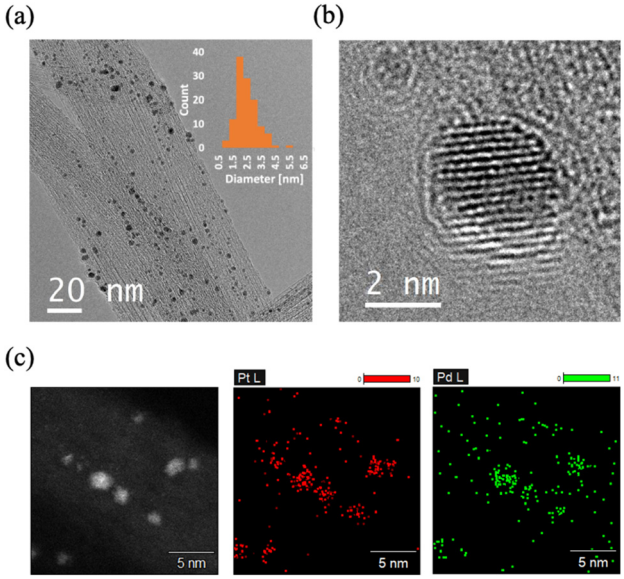

Fig. 2 Carbon-encapsulated PtPd alloy nanoparticles supported on SWCNTs (PtPd@C/SWCNT). (a) TEM image of PtPd@C/SWCNT (inset image: size histogram exhibiting the diameter distribution of carbon-encapsulated PtPd alloy nanoparticles). (b) High-resolution TEM image of PtPd@C/SWCNT shows that PtPd alloy nanoparticles are encapsulated by a carbon layer. (c) EDS measurement images of carbon-encapsulated PtPd alloy nanoparticles containing Pt and Pd.

surface of SWCNT bundles. The high-resolution TEM (HRTEM) images (Fig. 2(b)) revealed that these nanoparticles were encapsulated by amorphous carbon layers, approximately 1–2 layers thick, forming a shell. HRTEM analysis also indicated an average interatomic distance of 0.238 nm within the nanoparticle core, which is shorter than the Pt–Pt interatomic distance of 0.267 nm (SI Fig. S2(a and b)). This shorter distance suggests that the core metal nanoparticles are an alloy composed of both Pt and Pd atoms.[38] During the SP process, PtPd alloy nanoparticles were formed through the erosion of the PtPd alloy electrodes, followed by the diffusion of metal ions and the subsequent formation of metal clusters in the region between the two electrodes, driven by a bipolar-pulsed power supply.[27,39] Simultaneously, the amorphous carbon shells encapsulating the PtPd alloy nanoparticles were generated through the decomposition and recombination of reactive species, such as C_2, CH, H, and CN radicals, produced from the organic compounds present during the SP discharge.[40] A line profile analysis of the HR-TEM image revealed the thickness of a single-layer amorphous carbon shell to be 0.343 nm (SI Fig. S2(a and c)). In this study, nitrogen-containing DMF was used as the liquid precursor to facilitate the formation of N-doped carbon layers.[41] EDS measurements with elemental mapping confirmed that the synthesized core of the nanoparticles consisted of an alloy containing both platinum and palladium atoms (Fig. 2(c)). EDS area mapping performed on rectangular regions encompassing individual nanoparticles revealed a Pt to Pd ratio of approximately 79.4 : 20.6 (SI Fig. S3). This composition is consistent with the specified

composition of the PtPd alloy wire used in the synthesis, which contained 80% Pt.

XRD measurement of the synthesized PtPd@C/SWCNTs displayed diffraction peaks at 40.2°, 46.6°, 68.0°, and 81.8°, which are indexed to the (111), (200), (220), and (311) planes of a face-centered cubic (fcc) crystalline structure, respectively (JCPDS card no. 04-017-6714) (SI Fig. S4). Notably, the (111) peak for PtPd@C/SWCNT was slightly shifted to a higher 2θ angle compared to that of monometallic Pt nanoparticles (the Pt(111) peak for Pt/C is at 39.7°), indicating the formation of a PtPd alloy with a contracted lattice parameter and thus a shorter average interatomic distance within the nanoparticles. For reference, the pristine e-DIPS SWCNTs exhibited broad diffraction features around 43° and 44°, corresponding to the (100) and (101) planes of graphitic carbon.[42] Application of the Scherrer formula to the XRD data yielded an average crystallite size of 14.1 nm for the PtPd alloy nanoparticles.[43] This value was larger than the average particle size of 2.3 ± 0.8 nm observed by TEM, likely due to the presence of a small population of larger nanoparticles.[33] These larger nanoparticles, with sizes reaching several tens of nanometers, were occasionally observed on the SWCNT surface, likely formed due to irregular arc discharges between the electrodes during the synthesis. Efforts are currently underway to stabilize the plasma discharge and minimize the formation of these larger nanoparticles.

X-ray absorption near-edge structure (XANES) measurements at the Pt L_3-edge (SI Fig. S5(a)) showed that the PtPd@C/SWCNT catalyst exhibited spectra close to that of Pt foil, indicating that Pt predominantly existed in a metallic, low-oxidation state. This behavior was likely caused by electronic modulation from the SWCNT support and the nitrogen-containing carbon shell, where electron donation from the nitrogen species increased the electron density of Pt and stabilized its metallic state.[44] Consistently, Pt L_3-edge FT-EXAFS spectra (SI Fig. S5(b)) revealed a distinct Pt–N coordination in PtPd@C/SWCNT that is absent in Pt/C, demonstrating a significantly altered local Pt environment. In addition, the Pt–Pt peak shifts to a shorter radial distance, suggesting lattice compression, which may arise from Pt–Pd and enhanced Pt–Pt interactions induced by increased electron density.[26,45] These electronic and structural modifications contributed to the improved stability and catalytic performance of the PtPd@C/SWCNT catalyst for fuel cell applications.

RDE measurements of the separately synthesized electrocatalysts indicated the superior intrinsic ORR activity of the bimetallic catalyst (SI Fig. S6). PtPd@C/SWCNT alloy electrocatalyst exhibited a remarkably high specific activity (SA) of 946.8 μA cm^{-2}-Pt, which is approximately 1.8 times higher than that of Pt@C/SWCNT monometallic electrocatalyst (526.2 μA cm^{-2}-Pt) and 8.5 times higher than that of the commercial Pt/C standard (111.1 μA cm^{-2}-Pt). Despite this high intrinsic reactivity, the CV curves revealed that the hydrogen adsorption/desorption areas for both PtPd@C/SWCNT and Pt@C/SWCNT were significantly smaller than those of commercial Pt/C. This reduction in the active surface area suggested that the PtPd or Pt nanoparticles, synthesized *via* solution plasma in a DMF medium, were mostly encapsulated by a carbon shell (Fig. 2(b) and SI Fig. S7). This encapsulation likely restricted reactant access to the active sites, thereby reducing the ECSA. Furthermore, the relatively low ECSA and mass activity (MA) were attributed to the larger average particle diameters inherent to the solution plasma synthesis process, as confirmed by XRD measurements (SI Fig. S8). Consequently, while the MAs of PtPd@C/SWCNT (10.8 A g^{-1}-Pt) and Pt@C/SWCNT (29.8 A g^{-1}-Pt) currently remain lower than that of the commercial standard (66.3 A g^{-1}-Pt), the SWCNT-supported catalysts achieved a high SA with a substantially reduced platinum loading of approximately 6–7 μg cm^{-2}. This combination of enhanced intrinsic site reactivity and low precious metal loading underscores the synergistic role of the PtPd alloy and the e-DIPS SWCNT support in optimizing catalyst utilization for the ORR.

In the single cell test, SWCNT-based carbon-encapsulated electrocatalysts were employed as the cathode catalyst layer to evaluate their catalytic performance in the ORR. The cathode catalyst layer was fabricated using the membrane-filtration technique.[24] SDBS served as a dispersant to enhance the dispersion of the SWCNT-supported electrocatalysts. The catalyst solution, containing the SWCNT-based electrocatalyst, ethanol, SDBS, and Nafion solution, was sonicated for 15 minutes prior to filtration through a PTFE membrane filter. To achieve optimal catalytic performance, it is crucial to increase the dispersity of the catalyst to maximize surface area and porosity. The catalyst was then washed sequentially with acetone, methanol, and pure water to eliminate residual organic solvents, SDBS, and other impurities, as the presence of residual impurities, especially dispersants, can poison the catalyst and carbon support, thereby hindering performance. After drying overnight at 80 °C, the catalyst film on filter membrane was cut to an area of 1 cm^2, resulting in a Pt loading of 108 μm cm^{-2}. The anode catalyst layer was prepared by the drop-casting method using Pt/C (20 wt%) onto a Teflon sheet (1 cm^2) until the Pt loading reached 365 μg cm^{-2}. The SWCNT-based cathode catalyst layer and the Pt/C anode catalyst layer were coated onto a Nafion membrane (NRE-212) to form a membrane electrode assembly (*e.g.* PtPd@C/SWCNT-MEA) through hot-pressing at 140 °C and 1.5 MPa for 3 minutes. For comparison, a similar MEA (Pt/C-MEA) was fabricated using Pt/C as both the cathode and anode catalyst layers by employing the same hot-pressing technique. A conditioning treatment was conducted towards the fabricated MEAs to eliminate impurities, activate the catalyst surface, and increase the conductivity of the Nafion proton exchange membrane prior to any measurements. After *I–V* and CV measurements, a durability test was conducted by applying a triangular wave with potential between 1.0 and 1.5 V up to 30 000 cycles. The *I–V* and CV measurements were recorded during the durability test at 500, 1000, 2000, 5000, 10 000, 20 000, and 30 000 cycles.

Fig. 3a and c show the *I–V* curves of the Pt/C-MEA and PtPd@C/SWCNT-MEA, respectively, recorded during the durability test. The *I–V* curves indicate that the PtPd@C/SWCNT-MEA gained high performance after 500 cycles and maintained its performance up to 5000 cycles although the PtPd@C/SWCNT-MEA exhibited lower performance initially. The observed increase in current density during the first ~500 cycles can be attributed to our conditioning treatment of the

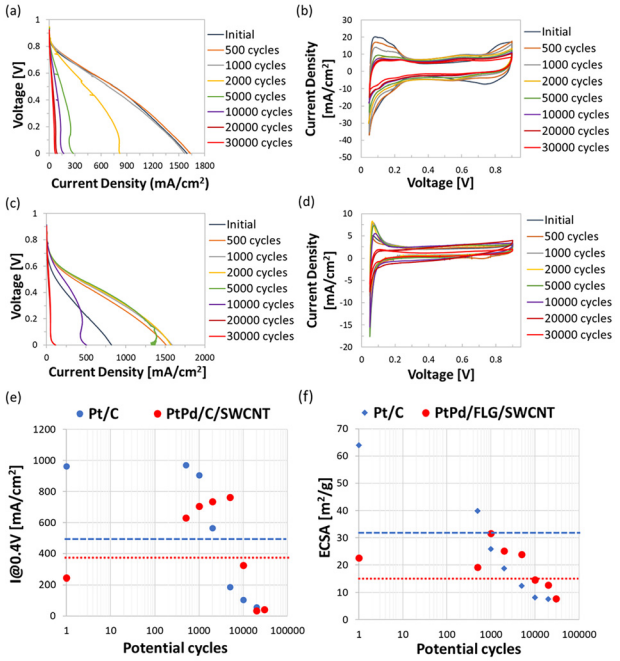

Fig. 3 *I–V* and CV plots of commercial Pt/C and PtPd@C/SWCNT during the durability test measured in a single-cell configuration using a fuel-cell test system. In the durability test, potential cycling was performed by applying a high-potential triangular wave between 1.0 V and 1.5 V with a period of 2 s per cycle. *I–V* measurements of MEAs with (a) commercial Pt/C and (c) PtPd@C/SWCNT as the cathode catalyst were recorded under the initial conditions and at 500, 1000, 2000, 5000, 10 000, 20 000, and 30 000 cycles during the durability test. CV measurements of MEAs with (b) Pt/C and (d) PtPd@C/SWCNT as the cathode catalyst were recorded under the initial conditions and at 500, 1000, 2000, 5000, 10 000, 20 000, and 30 000 cycles during the durability test. (e) Current density of *I–V* measurements using PtPd@C/SWCNT and Pt/C recorded at 0.4 V during the durability test. (f) the ECSA calculated from the CV curves of MEAs using PtPd@C/SWCNT and Pt/C as recorded during the durability test. The dashed lines in the graph correspond to the half value of the highest performance.

MEA before all measurements. However, this treatment was insufficient to completely oxidize or eliminate the remaining dispersant, the amorphous carbon, and CNT defects contained in the PtPd@C/SWCNT cathode catalyst layer under initial conditions. The elimination of these elements improved the mass transport of reaction products such as H_2O, leading to an enhanced current density. In contrast, the Pt/C-MEA retained its performance up to 1000 cycles prior to the significant decrease in performance that started at 2000 cycles.

Fig. 3e and f show the current density of *I–V* measurements using PtPd@C/SWCNT and Pt/C recorded at 0.4 V during the durability test and the calculated ECSA obtained from the CV measurements, respectively. At 0.4 V, the PtPd@C/SWCNT-MEA overlapped the performance the Pt/C-MEA at 2000 cycles and reached the highest current density of 762 mA cm^{-2} at 5000 cycles. Meanwhile, the Pt/C-MEA relatively maintained its performance up to 1000 cycles with the highest current density of 970 mA cm^{-2} at 500 cycles. The current density of Pt/C-MEA at 0.4 V decreased close to 50% of its best performance at 2000 cycles prior to the significant decrease that started at 5000 cycles. A similar trend was found on the ECSA value of the PtPd@C/SWCNT-MEA and Pt/C-MEA calculated from the CV graphs as shown in Fig. 3f. The ECSA value of the PtPd@C/SWCNT-MEA overlapped the ECSA value of the Pt/C-MEA at 1000 cycles and remained high up to 5000 cycles prior to the decrease close to 50% value of its best performance at 10 000 cycles. The ECSA value of the PtPd@C/SWCNT-MEA continued decreasing after 10 000 cycles. Meanwhile, the ECSA value of the Pt/C-MEA continuously decreased and reached a value less than 50% value of its best performance at the earlier step of 1000 cycles. The PtPd@C/SWCNT-MEA achieved a maximum power density of 316 mW cm^{-2}, which was lower than that of the Pt/C-MEA (389 mW cm^{-2}) (SI Fig. S9a and c). However, when normalized to the Pt loading on the cathode, the power density per mass of Pt was approximately three times higher for the PtPd@C/SWCNT-MEA (2.941 kW g^{-1}-Pt) compared to the Pt/C-MEA (1.067 kW g^{-1}-Pt) (SI Fig. S9b and d), demonstrating the high efficiency of the synthesized catalyst. The carbon shell encapsulation did not negatively impact its performance. Overall, these findings indicate that the synthesized PtPd@C/SWCNT exhibited superior durability, maintaining high performance up to 5000 cycles and retaining over 50% of its ECSA up to 10 000 cycles under the high-potential durability test designed to simulate the harsh conditions encountered during actual start-up/shut-down operations.

Following 30 000 cycles of the high-potential pulse durability test, significant agglomeration of Pt nanoparticles was observed in the Pt/C catalyst, resulting in the formation of larger particles (Fig. 4b). These high-potential pulses (1.0–1.5

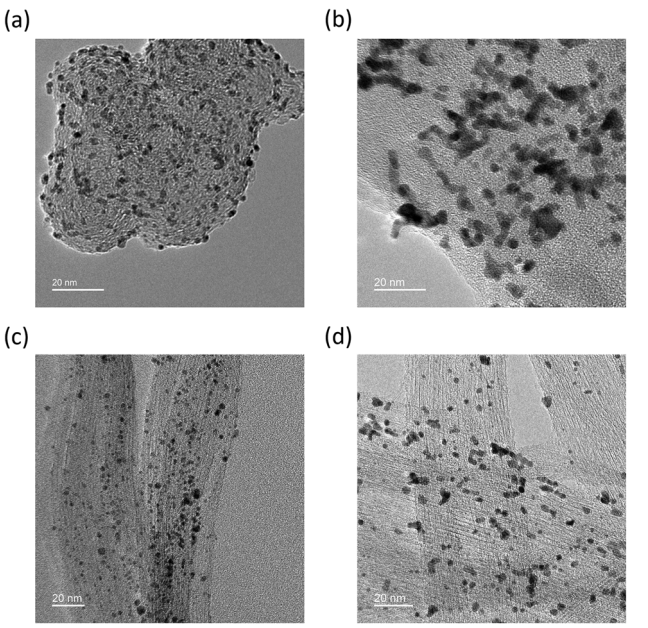

Fig. 4 TEM images of commercial Pt/C (a) before and (b) after the high-potential pulse durability test (1.0–1.5 V) of 30 000 cycles. TEM images of PtPd@C/SWCNT catalysts (c) before and (d) after the same durability test of 30 000 cycles.

V) induced Pt nanoparticle agglomeration through Ostwald ripening and coalescence mechanisms. Concurrently, the oxidation of the carbon support led to its structural collapse, reducing the surface area available for Pt dispersion and further exacerbating nanoparticle aggregation.[8,46] In contrast, the PtPd alloy nanoparticles in PtPd@C/SWCNT exhibited minimal agglomeration after the same durability test, as shown in Fig. 4d. The average size of these PtPd alloy nanoparticles, as determined using TEM, remained relatively constant at 2.2 ± 0.9 nm even after the test (SI Fig. S10). Notably, unlike our previous findings, no nanowire formation was observed on the SWCNT support after the durability test.[24] Furthermore, post-durability test EDS analysis confirmed the continued presence of both Pt and Pd within the catalyst nanostructures, indicating the stability of the alloy composition (SI Fig. S11). These results suggest that the carbon encapsulation effectively suppressed nanoparticle agglomeration under the applied high potential waves, despite the observation that some nanoparticles experienced a loss of their carbon shell due to undergoing oxidation under applied high potential during the durability test (SI Fig. S12). However, the high-potential start–stop cycling (1.0–1.5 V) degraded not only the carbon shell but also the membrane and ionomer, leading to secondary contamination effects; thus, the severe performance loss after extended cycling—especially after >10 000 cycles—reflects the combined degradation of multiple MEA components rather than carbon shell loss alone.

In addition, preliminary experiments were performed by employing PtPd@C/SWCNT and Pt@C/SWCNT as cathode catalysts to evaluate the advantage bimetallic catalysts over monometallic ones. *I–V* measurements exhibited the current density of PtPd@C/SWCNT-MEA at 0.6 V (119.1 mA cm^{-2}) with less Pt loading was higher than that of Pt@C/SWCNT-MEA (78.4 mA cm^{-2}), as shown in SI Fig. S13a. CV measurements also showed that the ECSA of PtPd@C/SWCNT-MEA (36.2 m^2 g^{-1}) was higher than that of Pt@C/SWNCT-MEA (29.9 m^2 g^{-1}) (SI Fig. S13b). Although the ECSA values were lower than those of commercial Pt/C due to carbon encapsulation, characteristic hydrogen adsorption/desorption peaks remained clearly discernible within the CV curves. A durability test, performed by applying high-potential triangular wave cycling to the MEAs, revealed that Pt@C/SWCNT possessed lower stability than its bimetallic counterpart, PtPd@C/SWCNT (SI Fig. S14). Specifically, the current density of the Pt@C/SWCNT-MEA significantly degraded at 5000 cycles. TEM observations confirmed that this degradation was partly driven by Pt nanoparticle aggregation and the partial breakdown of the carbon encapsulation (SI Fig. S15). These findings suggest that the superior current density and enhanced durability of PtPd@C/SWCNT are intrinsically linked to the synergistic effects and structural stability provided by the PtPd bimetallic configuration.

Raman spectroscopy exhibited no significant alterations in the spectra of pristine SWCNTs, the PtPd@C/SWCNT catalyst before the durability test, and the catalyst after the durability test (Fig. 5a). The loading of the PtPd alloy nanoparticles did

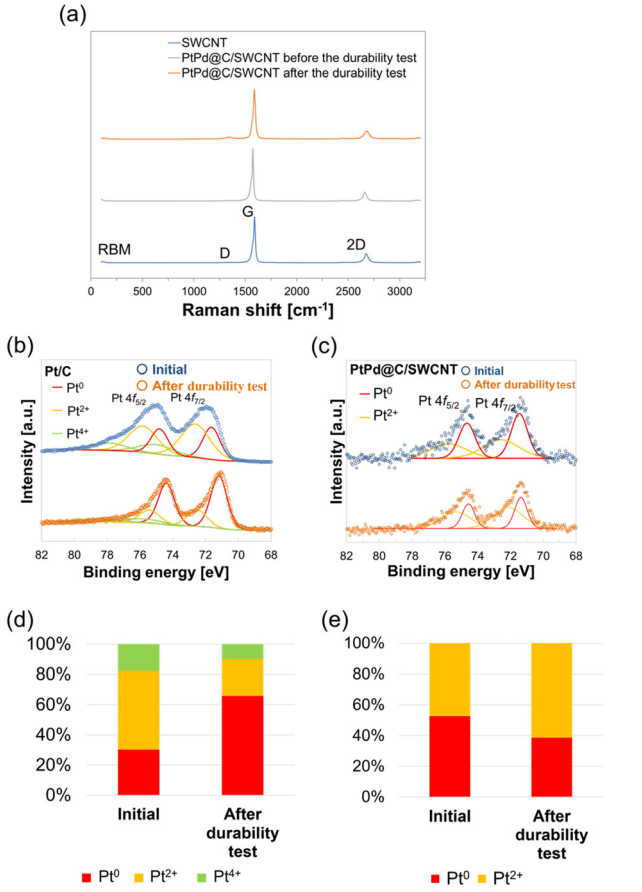

Fig. 5 (a) Raman spectra of pure SWCNT, PtPd@C/SWCNT before the durability test, and PtPd@C/SWCNT after the durability test. XPS Pt 4f spectra of (b) commercial Pt/C and (c) PtPd@C/SWCNT catalysts obtained before and after the durability test. The relative proportions of Pt^0, Pt^{2+}, and Pt^{4+} species in (d) Pt/C and (e) PtPd@C/SWCNT catalysts obtained before and after the durability test.

not substantially impact the SWCNT structure, as evidenced by the nearly unchanged I_d/I_g ratio of PtPd@C/SWCNT compared to that of pristine SWCNTs. This ratio, indicative of the degree of crystallinity, remained largely consistent (SI Table S1). Furthermore, the I_d/I_g ratio of PtPd@C/SWCNT showed only a slight increase after the high-potential pulse durability test. This minor increase was likely attributed to damage sustained by the carbon shells of some PtPd alloy nanoparticles during the test. This observation contrasts with our previous study using bare Pt nanoparticles without carbon encapsulation, where SWCNT oxidation at the Pt-SWCNT interface led to a decrease in crystallinity.[24] In the present case, the carbon shells encapsulating the PtPd electrocatalysts appear to inhibit the oxidation of the SWCNT support in the immediate vicinity of the nanoparticles, resulting from the Pt-catalysed carbon corrosion.[47,48] These findings collectively suggest that the combination of the SWCNT support and the carbon shell encapsulation of the catalyst provides remarkable resilience, preserving the crystallinity of the support and resisting corrosion even under the demanding high potential wave.

Cross-sectional SEM imaging was performed to examine the catalyst layer structure in the MEA after the durability test. The cathode catalyst layer of the MEA using PtPd@C/SWCNT maintained its structure, showing almost no change in thickness (SI Fig. S16a and b). In contrast, the cathode catalyst layer of the Pt/C-MEA experienced a 40–60% decrease in thickness (SI Fig. S16c). Higher magnification images of a cross-section of the Pt/C cathode catalyst layer revealed a collapse of its geometric structure, reducing the porous space within the carbon support (SI Fig. S17). This indicated that corrosion occurred during the durability test, leading to the oxidation of the carbon support and negatively impacting performance earlier in the test. These findings also demonstrated the superior durability of SWCNTs as a support material for the cathode catalyst compared to the commercially available carbon support.

The deconvoluted Pt 4f XPS spectra indicated a higher proportion of reduced metallic Pt (Pt^0, 52.6%) in the synthesized PtPd@C/SWCNT compared to commercial Pt/C (30.2%). This increased presence of metallic Pt in the synthesized catalyst was consistent with the result of the XANES measurements and was likely attributed to the less oxidized surface of the SWCNTs, the alloying with Pd, and the carbon encapsulation. XPS analysis exhibited that the Pt 4f spectra of the commercial Pt/C catalyst shifted toward lower binding energies following the durability test, as shown in Fig. 5a. As a result, the proportion of Pt^0 increased after the durability test (Fig. 5d). This shift to a more reduced state suggests significant agglomeration of Pt nanoparticles during the durability test. The observed particle growth likely resulted from combined Ostwald ripening and coalescence mechanisms, accompanied by concurrent oxidation of the carbon support material.[49] Conversely, the Pt 4f spectra of PtPd@C/SWCNT demonstrated a relatively stable reduced state even after the rigorous durability test. Initially, the Pt 4f binding energy in PtPd@C/SWCNT (71.46 eV) was lower than that in Pt/C (71.64 eV), indicating that Pt in the PtPd alloy had gained electrons. This electron enrichment is likely due to the higher electronegativity of Pt (2.28) compared to Pd (2.20).[50] However, the proportion of reduced Pt in PtPd@C/SWCNT after the durability test slightly decreased from 52.6% to 38.7% because a portion of nanoparticles experienced a loss of their carbon shell under applied high potential during the durability test, causing their surfaces to be partly exposed (Fig. 5e). In contrast, the proportion of the reduced Pt in Pt/C significantly increased from 30.2% to 65.8% due to the agglomeration. This result demonstrated that the carbon shell effectively protected the platinum-containing alloy catalyst at its core. The XPS analysis of the Pd 3d region in PtPd@C/SWCNT indicated that the carbon encapsulation and the SWCNT support effectively stabilized Pd in its reduced metallic state, evidenced by a binding energy of 335.7 eV (SI Fig. S18). However, the Pd 3d signal was absent after the durability test, possibly due to an uneven distribution of Pd nanoparticles in the cathode catalyst layer and the limited amount of sample obtained from post-durability test MEA. This uneven distribution was likely due to Ostwald ripening and coalescence of Pd, rather than Pt, during the high potential pulse durability test.[51,52]

4. Conclusions

Carbon-encapsulated PtPd alloy electrocatalysts supported on highly crystalline and pure e-DIPS SWCNTs were successfully synthesized using a rapid and industrially scalable solution plasma method. XRD and TEM measurements confirmed the formation of alloy nanoparticles with a carbon shell containing both Pt and Pd. When implemented as the cathode catalyst layer in a PEFC MEA, PtPd@C/SWCNT demonstrated superior durability, maintaining high performance for up to 5000 cycles and retaining over 50% of its electrochemically active surface area (ECSA) after 10 000 cycles under a high-potential durability test simulating harsh start-up/shut-down conditions. These results demonstrated that PtPd@C/SWCNT exceeded the durability targets set by DOE 2025 targets for catalyst supports. Post-durability TEM analysis confirmed that the PtPd alloy nanoparticles maintained their size, and the carbon encapsulation effectively inhibited agglomeration despite some loss of the shell on certain nanoparticles. Furthermore, Raman spectroscopy indicated that the combination of the SWCNT support and the carbon shell provided remarkable resilience, preserving the support's crystallinity and resisting corrosion under the demanding potential cycling tests. The PtPd@C/SWCNT cathode catalyst layer also exhibited negligible thickness change after 30 000 potential cycles. In contrast to Pt/C, the Pt 4f spectra of PtPd@C/SWCNT showed a more reduced state initially and largely retained this reduced state (71.4 eV) even after the rigorous durability testing. The synthesized bimetallic PtPd@C/SWCNT alloy electrocatalyst exhibited higher electrocatalytic performance and enhanced durability compared to the monometallic structure of Pt@C/SWCNT. These findings collectively highlight that the use of SWCNTs as a support and the carbon encapsulation of the electrocatalyst significantly enhance the durability of electrochemical catalysts for long-term operation. Such durable electrocatalysts represent a promising pathway towards realizing fuel cell devices with extended lifespans, especially for demanding applications such as heavy-duty vehicles.

Conflicts of interest

There are no conflicts to declare.

Data availability

The data supporting this article have been included as part of the supplementary information (SI). Supplementary information is available. See DOI: https://doi.org/10.1039/d5nr05265c.

Acknowledgements

We would like to thank Mr. Takeshi Hashimoto (Meijo Nano Carbon) for the carbon nanotubes and supporting us with

valuable data and discussion, and Dr. Takashi Watanabe for technical assistance in XAS measurements. This study was supported by the New Energy and Industrial Technology Development Organization (NEDO), Japan (JPNP20003).

References

1 M. L. Perry and T. F. Fuller, *J. Electrochem. Soc.*, 2002, **149**, S59–S67.
2 Y. Wang, K. S. Chen, J. Mishler, S. C. Cho and X. C. Adroher, *Appl. Energy*, 2011, **88**, 981–1007.
3 A. G. Olabi, T. Wilberforce and M. A. Abdelkareem, *Energy*, 2021, **214**, 118955.
4 R. L. Borup, A. Kusoglu, K. C. Neyerlin, R. Mukundan, R. K. Ahluwalia, D. A. Cullen, K. L. More, A. Z. Weber and D. J. Myers, *Curr. Opin. Electrochem.*, 2020, **21**, 192–200.
5 D. A. Cullen, K. C. Neyerlin, R. K. Ahluwalia, R. Mukundan, K. L. More, R. L. Borup, A. Z. Weber, D. J. Myers and A. Kusoglu, *Nat. Energy*, 2021, **6**, 462–474.
6 L. Yang, J. Shui, L. Du, Y. Shao, J. Liu, L. Dai and Z. Hu, *Adv. Mater.*, 2019, **31**, 1–20.
7 K. Kodama, T. Nagai, A. Kuwaki, R. Jinnouchi and Y. Morimoto, *Nat. Nanotechnol.*, 2021, **16**, 140–147.
8 L. Dubau, L. Castanheira, F. Maillard, M. Chatenet, O. Lottin, G. Maranzana, J. Dillet, A. Lamibrac, J. C. Perrin, E. Moukheiber, A. Elkaddouri, G. De Moor, C. Bas, L. Flandin and N. Caqué, *Wiley Interdiscip. Rev.: Energy Environ.*, 2014, **3**, 540–560.
9 H. Schmies, A. Bergmann, J. Drnec, G. Wang, D. Teschner, S. Kühl, D. J. S. Sandbeck, S. Cherevko, M. Gocyla, M. Shviro, M. Heggen, V. Ramani, R. E. Dunin-Borkowski, K. J. J. Mayrhofer and P. Strasser, *Adv. Energy Mater.*, 2018, **8**, 1–13.
10 S. Chung, K. Ham, S. Kang, H. K. Ju and J. Lee, *Electrochim. Acta*, 2020, **348**, 136346.
11 L. Huang, S. Zaman, X. Tian, Z. Wang, W. Fang and B. Y. Xia, *Acc. Chem. Res.*, 2021, **54**, 311–322.
12 F. Zhan, K. S. Hu, J. H. Mai, L. S. Zhang, Z. G. Zhang, H. He and X. H. Liu, *Rare Met.*, 2024, **43**, 2444–2468.
13 P. Ferreira-Aparicio, A. M. Chaparro, M. A. Folgado, J. J. Conde, E. Brightman and G. Hinds, *ACS Appl. Mater. Interfaces*, 2017, **9**, 10626–10636.
14 N. Macauley, D. D. Papadias, J. Fairweather, D. Spernjak, D. Langlois, R. Ahluwalia, K. L. More, R. Mukundan and R. L. Borup, *J. Electrochem. Soc.*, 2018, **165**, F3148–F3160.
15 M. Chisaka, *J. Mater. Chem. A*, 2024, **12**, 18636–18673.
16 S. Iijima and T. Ichihashi, *Nature*, 1993, **363**, 603–605.
17 M. F. L. De Volder, S. H. Tawfick, R. H. Baughman and A. J. Hart, *Science*, 2013, **339**, 535–539.
18 X. Zhao, A. Hayashi, Z. Noda, K. Kimijima, I. Yagi and K. Sasaki, *Electrochim. Acta*, 2013, **97**, 33–41.
19 E. Akbari and Z. Buntat, *Int. J. Energy Res.*, 2017, **41**, 92–102.
20 W. Zhang, P. Sherrell, A. I. Minett, J. M. Razal and J. Chen, *Energy Environ. Sci.*, 2010, **3**, 1286–1293.
21 M. A. Haque, R. Kurosaki, K. Oiwa, K. Ikeda, K. Sato, N. Nishi, H. Tachibana, T. Kawawaki and Y. Negishi, *ACS Appl. Energy Mater.*, 2024, **7**, 10317–10325.
22 T. Saito, S. Ohshima, T. Okazaki, S. Ohmori, M. Yumura and S. Iijima, *J. Nanosci. Nanotechnol.*, 2008, **8**, 6153–6157.
23 A. Nomura, in *Next Generation Batteries*, ed. K. Kanamura, Springer Singapore, Singapore, 2021, pp. 449–459.
24 M. Huda, T. Kawahara, J. H. Park, M. Kawasumi and Y. Matsuo, *ACS Appl. Energy Mater.*, 2023, **6**, 12226–12236.
25 Q. Chen, C. Y. Yu, Y. C. Zhai, T. Watanabe, M. Kawasumi, M. Huda and Y. Matsuo, *Small Methods*, 2025, **9**, 2500074.
26 Q. Chen, C.-Y. Yu, T. Watanabe, M. Kawasumi, M. Huda and Y. Matsuo, *Nanoscale*, 2025, **17**, 24503–24512.
27 G. Panomsuwan, T. Ueno, H. Yui, J. Nakamura and N. Saito, in *Molecular Technology: Materials Innovation*, ed. H. Yamamoto and T. Kato, Wiley-VCHVerlag GmbH& Co. KGaA, 1st edn, 2019, vol. 3, pp. 137–172.
28 C. Chokradjaroen, X. Wang, J. Niu, T. Fan and N. Saito, *Mater. Today Adv.*, 2022, **14**, 100244.
29 X. Hu, O. Takai and N. Saito, *Jpn. J. Appl. Phys.*, 2013, **52**, 01AN05.
30 P. Q. Phan, R. Naraprawatphong, P. Pornaroontham, J. Park, C. Chokradjaroen and N. Saito, *Mater. Adv.*, 2021, **2**, 322–335.
31 W. Wang, Z. Wang, J. Wang, C. J. Zhong and C. J. Liu, *Adv. Sci.*, 2017, **4**, 1–9.
32 Y. Gao, T. Uchiyama, K. Yamamoto, T. Watanabe, S. Tominaka, N. Thakur, R. Sato, T. Teranishi, H. Imai, Y. Sakurai and Y. Uchimoto, *ACS Catal.*, 2023, **13**, 10988–11000.
33 J.-H. Park, K. Kim, X. Wang, M. Huda, Y. Sawada, Y. Matsuo, N. Saito and M. Kawasumi, *J. Power Sources*, 2023, **580**, 233419.
34 K. Shinohara, A. Ohma, A. Iiyama, T. Yoshida and A. Daimaru, *ECS Trans.*, 2011, **41**, 775–784.
35 S. Stariha, N. Macauley, B. T. Sneed, D. Langlois, K. L. More, R. Mukundan and R. L. Borup, *J. Electrochem. Soc.*, 2018, **165**, F492–F501.
36 H.-S. Lin, D. Miyata, M. Yagisawa, M. Huda, S. Hashimoto, T. Hashimoto and Y. Matsuo, *Appl. Phys. Express*, 2022, **15**, 121001.
37 M. M. Rahman, H. Younes, N. Subramanian and A. Al Ghaferi, *J. Nanomater.*, 2014, **2014**, 102621.
38 J. Wu, S. Shan, H. Cronk, F. Chang, H. Kareem, Y. Zhao, J. Luo, V. Petkov and C. J. Zhong, *J. Phys. Chem. C*, 2017, **121**, 14128–14136.
39 G. Panomsuwan, N. Saito and T. Ishizaki, *Carbon*, 2016, **98**, 411–420.
40 G. Panomsuwan, N. Saito and T. Ishizaki, *Phys. Chem. Chem. Phys.*, 2015, **17**, 6227–6232.
41 P. Q. Phan, S. Chae, P. Pornaroontham, Y. Muta, K. Kim, X. Wang and N. Saito, *RSC Adv.*, 2020, **10**, 36627–36635.
42 K. Manna and S. K. Srivastava, *J. Phys. Chem. C*, 2018, **122**, 19913–19920.
43 B. D. Cullity, *Elements of X-ray Diffractions*, Addison-Wesley Publishing, Reading, MA, 1978.

44 B. Ni, P. Shen, G. Zhang, J. Zhao, H. Ding, Y. Ye, Z. Yue, H. Yang, H. Wei and K. Jiang, *J. Am. Chem. Soc.*, 2024, **146**, 11181–11192.
45 S. Ye, W. Chen, Z. Ou, Q. Zhang, J. Zhang, Y. Li, X. Ren, X. Ouyang, L. Zheng, X. Yan, J. Liu and Q. Zhang, *Angew. Chem., Int. Ed.*, 2025, **64**, e202414989.
46 S. Y. Huang, P. Ganesan, S. Park and B. N. Popov, *J. Am. Chem. Soc.*, 2009, **131**, 13898–13899.
47 N. Linse, L. Gubler, G. G. Scherer and A. Wokaun, *Electrochim. Acta*, 2011, **56**, 7541–7549.
48 Z. Zhao, L. Castanheira, L. Dubau, G. Berthomé, A. Crisci and F. Maillard, *J. Power Sources*, 2013, **230**, 236–243.
49 H. Daimon, S. I. Yamazaki, M. Asahi, T. Ioroi and M. Inaba, *ACS Catal.*, 2022, **12**, 8976–8985.
50 Y. Wu, X. Dai, J. Yu, Z. Song and L. Zhang, *ACS Appl. Nano Mater.*, 2024, **7**, 28619–28626.
51 A. Van den Bossche, N. Rodriguez Rodriguez, S. Riaño, W. Dehaen and K. Binnemans, *RSC Adv.*, 2021, **11**, 10110–10120.
52 D. A. J. Rand and R. Woods, *J. Electroanal. Chem.*, 1972, **35**, 209–218.